THE JOURNAL OF PHYSICAL CHEMISTRY C
A JOURNAL OF THE AMERICAN CHEMICAL SOCIETY

pubs.acs.org/JPCC

Article

Quantitative Spectroscopic Analysis of Water Populations in the Hydrated Nanopore Environments of a Natural Montmorillonite

Sabrina E. Kelch, Randall E. Youngman, Eric Ferrage, Jade J. Basinski, Jiaxing Wang, and Ludmilla Aristilde*

Cite This: J. Phys. Chem. C 2021, 125, 26552−26565

Read Online

ACCESS | Metrics & More | Article Recommendations | Supporting Information

ABSTRACT: Smectite clays are implicated in solute trapping in natural and engineered processes. Here we evaluated ^{23}Na solid-state nuclear magnetic resonance (NMR) and thermogravimetric analysis-coupled mass spectrometry (TGA−MS) for quantitative analysis of a hydrated natural Na-montmorillonite equilibrated at different relative humidity (RH). Using X-ray diffraction, we determined predominantly large-sized (∼1.55 nm) interlayers at 93% and 75% RH, 2:1 ratio of medium-sized (∼1.23 nm) to large-sized interlayers at 55% RH, and 2:1 ratio of small-sized (<0.96 nm) to medium-sized interlayers at 11% RH. Informed by simulated NMR of differently hydrated model Na-MONT systems, the experimental ^{23}Na NMR data revealed only fully hydrated Na^+ populations at 93% RH, a 2:1 ratio of partially hydrated (outer-sphere) to mineral-bound (inner-sphere) Na^+ populations at 55% RH and, remarkably, a near-equal proportion of these latter two Na^+ populations at 11% RH. Between 93% and 11% RH, the TGA−MS data captured a 57% increase in tightly bound waters (water loss at 100−300 °C) but only a 22% decrease in freely exchangeable waters (water loss below 40 °C). The addition of exogenous NaCl altered the aforementioned hydration behaviors, particularly at low RH. Our findings of persisting hydrated environments despite interlayer collapse implied water populations incongruent with predictions from smectite interlayer nanopore size distributions.

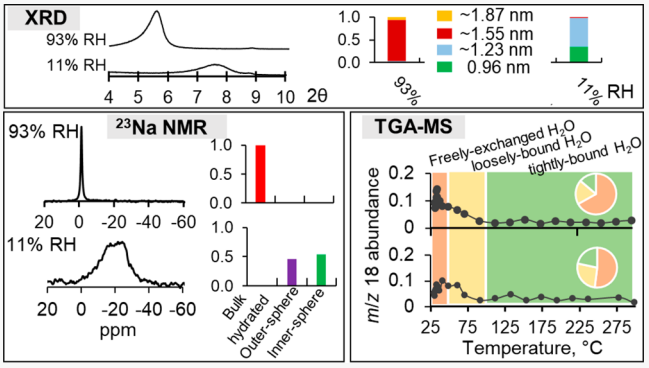

INTRODUCTION

Smectite-type clay minerals, which are commonly found in temperate soils and fine sediments,[1−4] are implicated in the retention of plant nutrients, natural organic matter, and inorganic and organic pollutants.[1−12] Smectite layers, which consist of 2:1 tetrahedral to octahedral sheets, have high cation exchange capacity ranging from 0.2 to 0.6 per half unit cell due to isomorphic substitutions in their structure (commonly Al^{3+} substituted for Si^{4+} in the tetrahedral sheet or Fe^{2+}/Mg^{2+} for Al^{3+} in the octahedral sheet).[2] Montmorillonite (MONT), a widely studied prototypical smectite clay, is characterized by having more Fe^{2+} or Mg^{2+} substituted into the octahedral sheet than Al^{3+} substituted into the tetrahedral sheet.[2] The isomorphic substitutions in smectite clays give rise to negative charges, which lead to interlayer swelling and moisture retention due to the hydration of the charge-compensating metal cations. The changes in the interlayer nanopore sizes of MONT and other smectites subjected to hydration or dehydration conditions are widely studied using moisture-dependent X-ray diffraction (XRD) measurements.[7,13−15] Regarding the specific behavior of the waters in the interlayer nanopore environments, much of what is known is from theoretical predictions based on molecular modeling simulations.[5,16−20] Largely lacking are direct experimental investigations to obtain a quantitative analysis of the hydration environments in the smectite interlayer nanopores.

Stepwise expansion of MONT interlayers as a result of increasing moisture has been studied extensively using XRD analysis of MONT samples equilibrated at different relative humidity (RH) conditions.[14] Using Bragg's law ($n\lambda = 2d \sin\theta$), the XRD data can be used to monitor changes in interlayer spacing (or d_{001}) by relating the placement of the 001 peak along the 2θ axis to d_{001}.[14,21,22] Modeling of the XRD profiles can unravel the proportions of different nanopore sizes within the matrix and the corresponding water layers (0W−3W) that can be accommodated within these nanopores depending on cation occupancy.[14,23−26] Water adsorption−desorption isotherms have revealed a three-step hydration pattern for Na-saturated MONT in response to increasing RH:

Received: June 21, 2021
Revised: November 14, 2021
Published: November 26, 2021

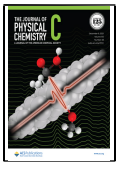

https://doi.org/10.1021/acs.jpcc.1c05462
J. Phys. Chem. C 2021, 125, 26552−26565

monolayer water adsorption from 20% to 50% RH, a bihydrated condition from 50% to 80% RH, and trihyrated water adsorption above 80% RH.[7,22,24,27−32] Accordingly, in a fully Na^+-exchanged smectite, an interlayer size or thickness of less than 1 nm has been described as a dehydrated interlayer, 1.18−1.29 nm as a monohydrated (1W) interlayer, 1.45−1.58 nm as a bihydrated (or 2W) interlayer, and 1.80−1.95 nm as a trihydrated (or 3W) interlayer.[15,33,34] We expect that the presence of indigenous Ca^{2+} and K^+ in the natural Na-MONT would alter these aforementioned strict distinctions of the different hydrated states. Use of XRD can thus reveal moisture-dependent nanopore size dynamics within the smectite. However, XRD analysis does not directly probe the water molecules or the arrangement of water populations hydrating the smectite nanopores.

Fourier-transform infrared spectroscopy (FTIR) can be used to evaluate water−smectite associations in hydrated minerals by monitoring the exchangeable water−OH vibrational band (~3530−3050 cm^{-1}) relative to −OH bond vibration (~3615 cm^{-1}) of the mineral structure.[7,35,36] Monitoring of the exchangeable water band centered at ~3400 cm^{-1} as a function of different moisture conditions has been used to discern the relative amount of water associated with the MONT interface with respect to the static mineral structure OH vibration band at ~3615 cm^{-1}.[24] Therefore, FTIR has been useful to probe the hydration condition within a smectite clay, but high resolution probing of different water populations still remains elusive.[24]

As a complement to XRD and FTIR data, solid-state ^{23}Na nuclear magnetic resonance spectroscopy (NMR) can provide additional insights by distinguishing several Na^+ hydration environments as a proxy method for identifying different moisture environments within the mineral matrix.[37−40] Prior studies with phyllosilicate minerals subjected to different moisture conditions reported a progressively broader ^{23}Na NMR resonance peak that was shifted to a more negative ppm during dehydration.[41−46] Specifically, in MONT, a sharp resonance peak around 0 to −2 ppm was attributed to a fully hydrated, spherical Na^+ environment whereas Na^+ in low moisture or dehydrated environments was represented by broad peaks around −20 to −25 ppm.[37−40] The ^{23}Na NMR resonances of samples under moisture-controlled conditions can be used to investigate further the different Na^+ hydration populations and identify, for instance, the relative abundance of inner-sphere and outer-sphere complexed Na^+ populations.[47] Combining information from ^{23}Na NMR and XRD measurements of MONT equilibrated at different hydration conditions can thus reveal useful insights into the hydration environments in MONT. However, these techniques still represent indirect measurements of water behavior and do not elucidate the extent of mobility versus trapping of the different water populations within the mineral matrix.

Thermogravimetric analysis (TGA) has long been used to study mineral dehydration and associated water content through high-precision mass loss monitoring from aluminosilicate minerals as a function of increasing temperature.[47−56] Most TGA studies attributed one region (0−300 °C) to the loss of MONT hydration waters (free water, metal cation hydration, mineral-bound water) and another region (above 300 °C, particularly 500−800 °C) to the dehydroxylation of the mineral structure.[47,49−57] Further attempts at discriminating between different water populations have highlighted three distinct subregions in accordance with the different temperature ranges of water loss between 30 and 300 °C.[49] First, easily removable waters at relatively low temperatures were termed free waters or weakly bound waters, whereas water losses at relatively higher temperatures were attributed to the consecutive loss of interlayer surface-bound waters and hydrated waters of interlayer cations.[49,56] A major assumption in these TGA analyses was that mass loss can only be attributed to water loss along a certain temperature range. However, this assumption is not appropriate, for instance, in the presence of organic or inorganic impurities in the mineral matrix, especially in the case of natural mineral samples that can thermally degrade at less than 300 °C.[51,58−62] The coupling of TGA with mass spectrometry (TGA−MS) has been used for the monitoring of water-specific mass loss by quantifying the loss of the water ion [mass over charge (m/z), 18].[50,56]

Here, in relation to the nanopore hydration states predicted by moisture-dependent XRD, our objective was to evaluate the combined application of ^{23}Na NMR and TGA−MS to perform a quantitative analysis of the hydration properties of a natural Na-MONT. We tested two hypotheses: first, that MONT dehydration will result in a shift from hydrated Na^+ populations to inner-sphere Na^+ complexed on the mineral surface; second, that the dehydration of the MONT interlayer will result in a decrease in the interlayer nanopore size accompanied by trapping of mineral-associated hydration waters. First, we obtained moisture-dependent XRD data and performed subsequent quantitative modeling of these data to determine nanopore size dynamics along a RH gradient. Using MONT samples equilibrated at different RH conditions, we determined the Na^+ hydration environment using ^{23}Na NMR and quantified the loss of different water populations with TGA−MS measurements. We interpret our data in relation to the predicted nanopore environment of MONT determined by XRD. To examine the effects of NaCl loading on the measured data, we performed experiments of MONT loaded with different concentrations of exogenous NaCl. The work presented here utilizes complementary spectroscopic techniques to probe multiple facets of the mineral hydration environment in MONT at different moisture conditions. We discovered that TGA−MS and ^{23}Na NMR data captured unique behavior of the Na-associated and mineral-associated water populations, which was not captured by XRD nanopore size dynamics.

MATERIALS AND METHODS

Materials. The clay mineral, SWy-2 Wyoming Na-MONT, was obtained from the clay repository of the Clay Mineral Society[57] (West Lafayette, IN, U.S.A.) and used as received. The structural formula of the purchased MONT[57] was reported as $(Ca_{0.12}Na_{0.32}K_{0.05})(Al_{3.01}Fe(III)_{0.41}Mn_{0.01}Mg_{0.54}Ti_{0.02})(Si_{7.98}Al_{0.02})O_{20}(OH)_4$, with an octahedral sheet charge of −0.53 and a tetrahedral sheet charge of −0.02. All other chemicals were purchased, analytical grade, from ThermoFisher Scientific (Waltham, MA, U.S.A).

Sample Preparation. By use of a 50 mL polypropylene tube with a conical bottom, MONT samples were prepared by shaking (240 h) 15 g L^{-1} MONT in solution with varying NaCl concentrations: 0 mM, 1 mM, 10 mM, and 100 mM. All solutions, which were prepared with Milli-Q purified water, were adjusted to pH 6.5 using small aliquots of 1 M HCl. Two additional samples were prepared with 20 mM of the buffer $NaC_2H_3O_2$ or $NaHCO_3$ in addition to 100 mM NaCl in

https://doi.org/10.1021/acs.jpcc.1c05462
J. Phys. Chem. C 2021, 125, 26552−26565

solution. Following shaking, the samples were centrifuged (2000*g*, 20 min), and after removal of the supernatant, the mineral slurries were equilibrated (for at least 72 h) at different relative humidity (RH) conditions: 11%, 33%, 55%, 75%, or 93% RH. These different RH conditions were maintained by using salt chambers with, respectively, LiCl, $MgCl_2$, $Mg(NO_3)_2$, NaCl, and KNO_3 in a supersaturated solution in the chambers.[63] Chambers had an inside diameter of 180 mm and were purchased from Grainger Lab Safety Supply (Lake Forest, IL U.S.A).

An additional sample of MONT with the highest NaCl loading (100 mM), as well as the MONT samples loaded with Na^+ buffers, was subjected to a washing step. Washing was completed by resuspending the MONT slurry in pure Milli-Q water and shaking for 24 h followed by centrifugation (2000*g*, 20 min); this procedure was repeated three times for all samples demarcated "washed". Reference NaCl (as purchased) samples for the solid-state ^{23}Na NMR analyses were prepared following the same procedure as above including RH equilibration. The NaCl reference sample at 93% RH was run using liquid-state ^{23}Na NMR due to the low viscosity of that sample.

XRD Measurements and Modeling of MONT Nanopore Abundance. The XRD profiles were recorded at 93% RH followed sequentially by 75%, 55%, 33%, and 11% RH after a 1 h *in situ* equilibration in the sample holder at each RH value (using Bruker constant humidity setting). The XRD profiles were recorded with a Bruker D8 Advance powder X-ray diffractometer operated at 40 kV voltage and 40 mA current. The XRD was operated with a Göebel Mirror and Soller 0.2° optic as well as an SSD160_2 detector used in 0D mode. A temperature of 25 °C in the XRD sample chamber was maintained throughout collection. The X-ray diffractometer was equipped with a CHC+ humidity-controlled chamber (Anton Paar, Graz, Austria) coupled to a ProUmid MHG-32 modular humidity generator (ProUmid, Ulm, Germany) and an Anton Paar Eurotherm TCU110 temperature control unit. Scanning parameters were set at 0.01° 2θ step size with a 1 s counting time per step over a 2−12 2θ Cu Kα angular range (λ = 1.5418 Å). Diffrac.suite software from Bruker was used for measurement and analysis including Diffrac.Eva V5.2 for postcollection analysis.

The experimental XRD patterns of MONT were modeled in the 3−11° 2θ Cu Kα range using the algorithms developed by Sakharov and co-workers[33] to determine the relative abundance for small-sized pores (interlayer spacing of 0.96−1.07 nm), medium-sized pores (1.18−1.29 nm), large-sized pores (1.45−1.58 nm), and the largest sized pores (1.8−1.95 nm).[14] Instead of using the traditional hydrated state definition (i.e., 0W, 1W, 2W, 3W), the nanopore sizes were considered to describe our interlayer distribution because a pure Na-montmorillnite was not used here. The natural Na-MONT, which primarily contains Na^+, also contains other metal cations as counterions that can exhibit slightly different hydration states. By use of Bragg's law, $n\lambda = 2d \sin\theta$, interlayer d-spacing can be related to the placement of the d_{001} peak along the 2θ axis.[14] The approach adopted to model the XRD nanopore abundance, which has been explained in detail elsewhere,[15] is described briefly here. One structure containing one or multiple different layer types was first used to reproduce the 001-reflection region as much as possible. When necessary, additional interstratified contributions containing larger interlayer sizes were added to the structure model. In all samples, the quantification of nanopore abundance was determined from the consideration of three-layer types associated with different interlayer sizes. Only the change of proportion of these layers in the different samples was responsible for the good fit obtained for all patterns. For all patterns, structural parameters, such as the number of and relative abundance of the different interstratified structures (limited to four here), their composition (relative proportions of the different layer types), and the mean number of layers in the coherent scattering domain size along the c*-axis, were adjusted to fit the experimental XRD pattern. The mean number of layers in the coherent scattering domain sizes was found to range between 12 and 7.5 layers for all patterns investigated and showed a systematic increase with decreasing RH values, in agreement with previous studies of smectite structure evolution along water desorption isotherms.[14,15]

TGA−MS Analysis of Water Populations. The TGA analyses were conducted with a Netzsch STA 449 F3 Jupiter simultaneous thermal analysis (STA) instrument. Centrifuged clay slurry samples after RH equilibration as described above were placed in Al_2O_3 crucibles and measured under ultrahigh purity helium gas (50 mL/min). The buoyancy effect of helium was corrected for by measuring the empty crucible under the same measurement conditions used for the samples. Temperature was increased at a rate of 20 °C/min from 35 to 1500 °C, and gases were transferred to the GC/MS instrumentation via a heated (250 °C) transfer line. An Agilent Technologies 7890A GC system equipped with a nonpolar capillary column (Agilent J&B HP-5 packed with (5% phenyl)-methylpolysiloxane) coupled with a 5975 MSD spectrometer was used for the analyses of the gases released from the samples. Gas injections were triggered from the beginning of the heating cycle, and 0.25 mL of gas was sampled from the gases released by the compound and carrier gas (helium). Performance of the thermobalance of the STA was verified by using a certified sample of calcium oxalate monohydrate (European Pharmacopoeia Reference Standard) up to 1000 °C. Ion chromatographic data were analyzed via enhanced ChemStation software (MSD ChemStation F.01.03.2357) from Agilent Technologies, Inc. (Santa Clara, CA U.S.A). Thermogravimetric analyses (TGA, DTA, and their first-order derivatives DTGA and DDTA) were performed using NETZSCH Proteus thermal analysis software, version 8.0.1 (Selb, Germany).

Solid-State ^{23}Na NMR Analysis of Na^+ Hydration Environments. The ^{23}Na magic-angle spinning NMR measurements were performed for the different RH-equilibrated samples (93%, 75%, 55%, and 11% RH) using an 11.7 T spectrometer (Agilent, DD2) with widebore superconducting magnet and a 3.2 mm MAS NMR probe (Varian). The resonance frequency of ^{23}Na at this magnetic field was 132.19 MHz. Samples were loaded into 3.2 mm outer diameter zirconia rotors that contained tight-fitting Torlon spacers and end-caps. Sample spinning was computer-controlled at 20 000 ± 1 Hz. These data were collected by direct polarization, using a short radio frequency pulse width of 0.6 μs, corresponding to a $\pi/12$ tip angle, and a 60s recycle delay between acquisitions. These measurement conditions, along with the collection of 200−2000 transients, were sufficient to collect quantitative NMR spectra with adequate signal-to-noise levels. All spectra were referenced to an external shift standard of dilute aqueous NaCl (0.0 ppm) and processed using commercial software with 100 Hz line broadening.

https://doi.org/10.1021/acs.jpcc.1c05462
J. Phys. Chem. C 2021, 125, 26552−26565

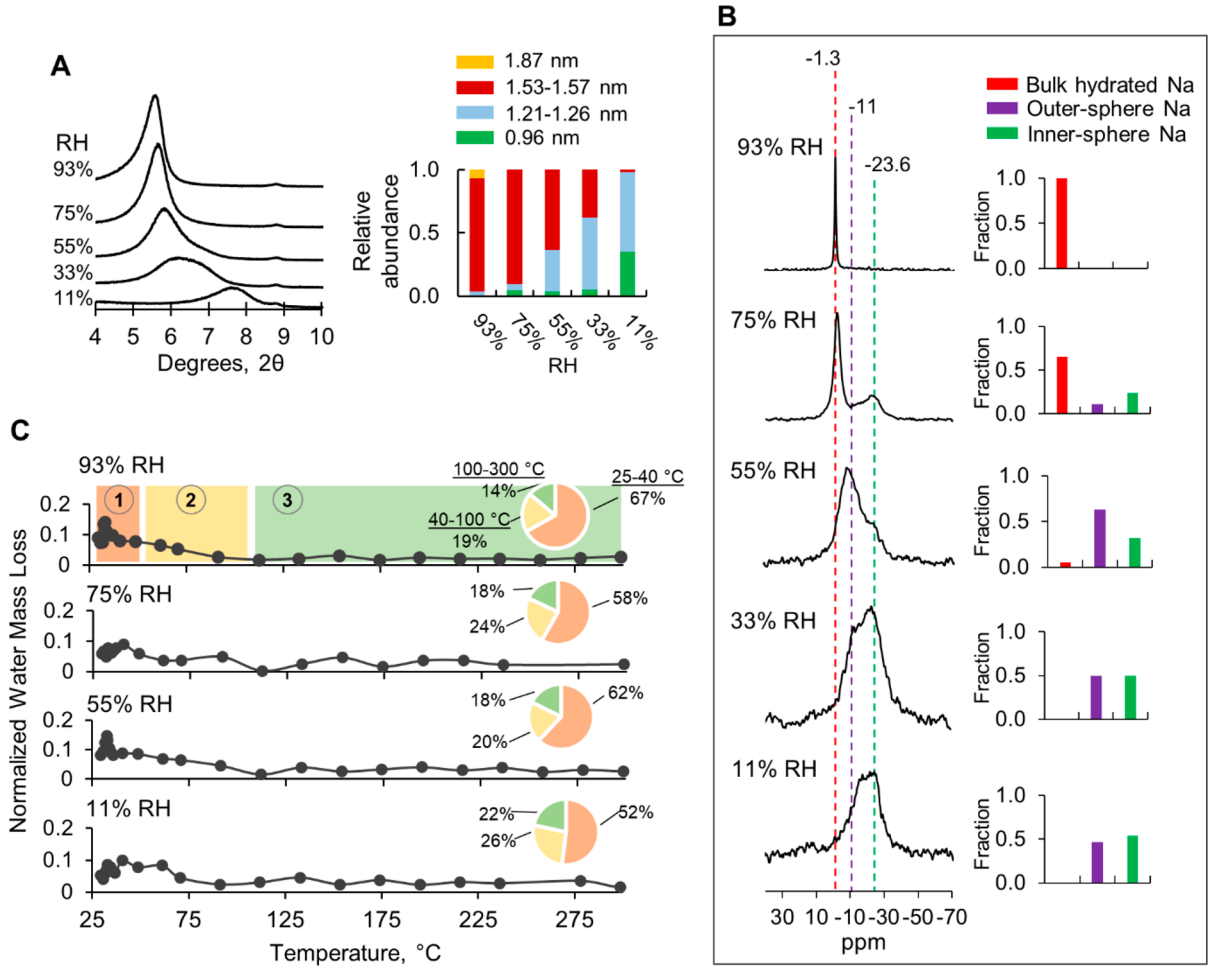

Figure 1. Spectroscopic analysis of a natural Na-MONT. (A) Moisture-dependent X-ray diffraction profiles and modeling of nanopore distribution for MONT control (no added sodium). The different interlayer sizes used in the modeling are represented by green bars (0.96 nm), light blue bars (1.21−1.26 nm), dark red bars (1.53−1.57 nm), and yellow bars (1.87 nm). (B) RH-dependent solid-state ^{23}Na NMR resonances of MONT control with peak distribution abundances from Mnova 14.2 line fitting. (C) Monitoring ion abundance (m/z 18 − H_2O) for MONT control. Spectra were sectioned into freely exchangeable water T = 25−40 °C, loosely bound water T = 40−100 °C, and tightly bound water T = 100−300 °C and normalized for structural OH loss (300−800 °C). Pie charts show the percent of the total 25−300 °C normalized mass loss within each section. Y-axis reflects normalized mass loss in mg.

For all 33% RH-equilibrated samples, data were recorded on a 400 MHz Bruker Avance III HD NMR spectrometer with a 4 mm HX probe. Bruker pulse program hpdec was used for the ^{23}Na NMR experiments along with Bruker Topspin 3.6.2 software for data collection. The frequency of ^{23}Na was 105.5737 MHz. The 90° pulse width was calibrated to 1 μs at 120W. A 30s recycle delay was used. The magic angle spinning rate was set to 10 000 Hz. Solid-state ^{23}Na NMR spectra were referenced to an external solid NaCl peak at δ 7.21 which was converted to a 1 M NaCl peak at δ 0.0 ppm. The number of scans was set to 4. Line fitting of all NMR spectra was completed using MestReNova software, version 14.1.1 (Santiago de Compostela, Spain). Line fitting of the ^{23}Na NMR spectra revealed four distinctive populations: crystalline NaCl or precipitated NaCl which encompasses resonances between approximately 6.25 and 7.22 ppm, bulk hydrated Na^+ with peaks between −0.36 and −2.62 ppm, outer-sphere Na^+ between −4.9 and −15.71 ppm, and inner-sphere dehydrated Na^+ from −19.35 to −25.38 ppm (SI Table E). Other than the environment of Na^+ fully hydrated by water or in perfectly cubic symmetry such as in crystalline NaCl, ^{23}Na NMR lineshapes for rigid environments normally exhibit second-order quadrupolar line broadening under magic-angle spinning NMR. The shape of these peaks was approximated using Mnova 14.2 default line fitting settings which used generalized Lorentzian functions to estimate peak positions and areas. The measured shifts at 11.7 T are similar to those reported at other magnetic field strengths, including the lower field data at 9.4 T for all 33% RH samples reported in this study. The peaks are slightly broadened at lower field but otherwise consistent with small quadrupolar coupling constants for all ^{23}Na NMR data and thus can be approximated using the fitting approach described herein

Simulated ^{23}Na NMR. Simulations of different populations of Na^+ with the MONT interlayers were conudcted using Biovia's Materials Studio and Discovery Studio software packages.[64,65] The simulated clay used was based on a Wyoming-type montmorillonite with an average stoichiometry of $Na_{0.5}(Si_8)(Al_{3.5}Mg_{0.5})O_{20}(OH)_4$ and prepared as previously detailed.[5] To reduce computation requirements, the adsorption simulation was conducted with a unit cell, which contained a total charge of −4 based on random isomorphic substitutions of Al^{3+} to Mg^{2+} in the octahedral sheet. The CLAYFF model was used to generate the initial partial charges

https://doi.org/10.1021/acs.jpcc.1c05462
J. Phys. Chem. C 2021, 125, 26552−26565

of MONT, and the single-point charge model was used for water.[66,67] The Na^+ and atomic interactions were described using the condensed-phase optimized molecular potentials for atomistic simulation studies (COMPASS) force field (version II).[68] This force field has been shown to model appropriately the hydration of metal cations and interaction of MONT with organic and inorganic adsorptives.[69−71] Four interlayer nanopore environments with different Na^+ populations were modeled: a fully hydrated Na-MONTat 1.55 nm d_{001} with 4 Na^+ and 40 waters, and two partially hydrated Na-MONT at with 4 Na^+ and 20 waters or at 1.24 nm d_{001} with 4 Na^+ and 10 waters, and dry Na-MONT at 0.96 nm d_{001} with 4 Na^+. Each of these four systems were generated using the adsorption locator module in Materials Studio as previously described.[72]

The CASTEP NMR module of Materials Studio was employed to calculate the chemical shielding tensor and electric field gradient for the Na^+ in systems mentioned above.[73,74] Periodic cells were generated from the prepared fully hydrated Na^+ and Na^+-MONT systems using the crystal building function in Materials Studio. The systems were described using the Perdew−Burke−Ernzerhof generalized gradient approximation functional with the TS method for DFT-D correction, which has been shown to be effective in crystal systems.[75,76] The energy cutoff used for calculation was 517 eV, and the self-consistent field (SCF) energy cut off was 2×10^{-6}eV with a maximum of 100 SCF cycles. The "on the fly" generated (OTFG) ultrasoft pseudopotential and the Koelling−Harmon relativistic treatment were used to maintain high accuracy while also being compatible with NMR chemical shift computation, as calculation for NMR parameters requires OTFG.[77,78] The NMR.magres file from the CASTEP output was imported to MagresView 1.6.2 for spectrum visualization.[79] Only the Na^+ signal was chosen for display. The chemical shift of fully hydrated Na^+ was calibrated to −1.3 ppm as informed by the experimental ^{23}Na NMR data; the chemical shift reference was used to calibrate the peak of Na^+ in the other partially hydrated Na-MONT systems. Line broadening was applied to the simulated NMR peaks.

RESULTS AND DISCUSSION

Moisture-Dependent Spectroscopic Analysis of a Natural Na-MONT. The XRD data obtained with MONT alone showed a typical evolution of XRD profile shape in response to dehydration (Figure 1A). At 93% RH, there was a narrow and symmetrical d_{001} peak at low 2θ values, followed by increased peak breadth and a shift to higher 2θ values between 55% and 11% RH (Figure 1A). The shift of the peak from low to high 2θ values between 93% and 11% RH reflected a collapse of the interlayer nanopore size for MONT alone (Figure 1A), which was characterized by a 67% decrease in the nanopore width (from 1.593 to 1.160 nm interlayer thickness or from 0.643 to 0.21 nm pore width after mineral lattice subtraction) (Table 1). We also observed an over 150% increase in the full width at half-maximum value (fwhm) between 93% RH and 11% RH for MONT alone, whereby the largest fwhm increase occurred between 55% and 33% RH (a 72% increase) (Figure 1A; Table 1). This increase in fwhm was indicative of the presence of multiple nanopore sizes at low RH conditions compared to the relatively homogeneous nanopore size distribution at 93% RH (Figure 1A; Table 1).[7] The change in the heterogeneity of nanopore sizes was captured quantitatively by nanopore modeling based on the XRD data (Figure 1A; SI Figure D). At 93% and 75% RH, ∼90% of the mineral interlayers were 1.53−1.57 nm (large-sized nanopore), and there were only minor contributions from other sizes (Figure 1A). However, at 55% and 33% RH, there was an increased proportion (33% and 57%, respectively) of the 1.21−1.26 nm mineral interlayers (medium-sized nanopore) (Figure 1A). At 11% RH, the two major constituents were the medium-sized nanopores (63% of total) and the dehydrated small-sized nanopore (0.96 nm, 35% of total) (Figure 1A). This evolution from predominantly large-sized nanopores to primarily a mixture of medium-sized and small-sized nanopores implicated a shift from bihydrated nanopores to a mixture of monohydrated and dehydrated nanopores.[7,14]

Table 1. Results from Experimental X-ray Diffraction Patterns of MONT Control[a]

% RH	d_{001}	Δd	fwhm
93	1.59		0.587
75	1.57	0.022	0.590
55	1.52	0.076	0.860
33	1.40	0.19	1.48
11	1.16	0.43	1.01

[a]RH, relative humidity (RH) for *in situ* moisture-dependent X-ray diffraction measurements; fwhm, full width at half-maximum (2θ°); d_{001}, the basal spacing of the clay layers shown in nm; Δd, difference in interlayer spacing relative to the 93% RH condition (nm).

To capture differently hydrated Na^+ environments experimentally, we conducted ^{23}Na NMR measurements on Na-MONT equilibrated at different moisture conditions (Figure 1B). To aid in the structural interpretation of the experimental ^{23}Na NMR measurements, we obtained simulated NMR spectra following the molecular modeling of four different hydrated Na-MONT systems: a fully hydrated Na-MONT system, a fully dry Na-MONT system, and two partially hydrated Na-MONT systems (with 50% and 25% of the water population in the fully hydrated system) (Figure 2). Expectedly, with decreasing water abundance in the simulated Na-MONT interlayers, there was a decrease in the amount of coordinated water O atoms around Na^+: four water O atoms in the fully hydrated Na-MONT and three water O atoms in the two partially hydrated interlayers (Figure 2). Decrease in water O coordination was eventually accompanied by an incease in clay O coordination: from 1 clay O atom in the two partially hydrated waters to 3 to 7 clay O atoms in the dry interlayer (Figure 2). This decrease in hydrated waters along with increased interactions with the clay basal surface led to a change in the simulated ^{23}Na NMR signal peak, from being at −1.3 ppm to −9.5 ppm (Figure 2). For our experimental data, we obtained ^{23}Na NMR data with the natural Na-MONT equilibrated at 93%, 75%, 55%, 33%, and 11% RH (Figure 1B). The NMR spectrum obtained with our high-moisture (93% RH) matched well in both peak shape and peak position to a prior report of Na-MONT at 34.6% water content by weight and subsequently revealed a similar broadening and shift to more negative ppm values when the sample was measured under dehydrated conditions, as demonstrated by our simulation data.[80] The ^{23}Na NMR data were congruent with prior reports measuring dry Na-MONT, in both peak breath and peak position,[47,80] and were also in agreement with prior findings on Na-hectorite measured at both dry and 50% RH conditions.[40]

Informed by our simulation predictions obtained here and previous studies,[37−40] the ^{23}Na NMR spectra at the end-

https://doi.org/10.1021/acs.jpcc.1c05462
J. Phys. Chem. C 2021, 125, 26552−26565

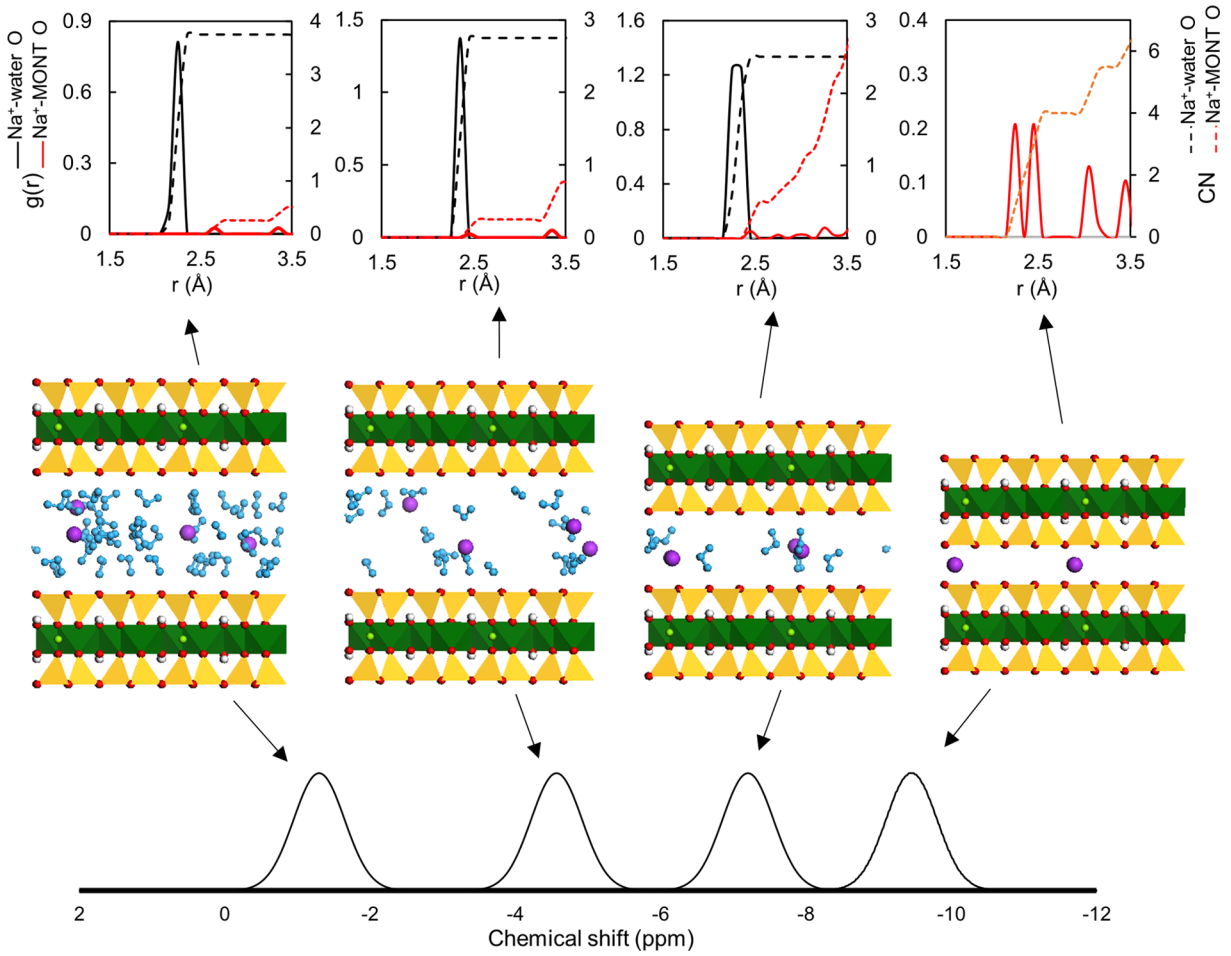

Figure 2. Molecular modeling and NMR simulation for Na^+ in different hydrated Na-MONT interlayers. From left to right: Fully hydrated Na-MONT at 1.55-nm d_{001}, partially hydrated Na-MONT at 1.55-nm d_{001}, partially hydrated Na-MONT at 1.24-nm d_{001}, and dry Na-MONT at 0.96-nm d_{001}. Corresponding ^{23}Na NMR chemical shift from left to right: −1.3 ppm, −4.57 ppm, −7.20 ppm, and −9.45 ppm. The radial distribution function [RDF, $g(r)$] of each system is shown on top. Color codes for atoms and molecules in the model Na-MONT interlayers: purple (Na), green (aluminum), red (oxygen in MONT), gray (hydrogen in MONT), light blue (water).

member RH conditions (93% RH and 11% RH) were used to categorize hydrated and dehydrated Na^+ resonances in the MONT control sample. Previously,[47] three Na^+ populations have been delineated (from most to least hydrated): a fully hydrated Na^+ (reminiscent of Na^+ found in liquid samples)[37] in a symmetrical fully hydrated environment with its first hydration sphere of up to 6 water molecules as well as a second or more hydration spheres separating it from the silicate sheet, an outer-sphere complexed or partially hydrated Na^+, and a dehydrated Na^+ that has lost hydration waters and is involved in inner-sphere complexation with the oxygen of the silicate sheet (Figure 2). Here the ^{23}Na NMR data matched well with prior reports that hydrated samples have sharp peaks indicative of fully hydrated Na^+ environments and that dehydrated samples exhibited a broader resonance.[37−40]

The application of line fitting to the ^{23}Na NMR resonances provided quantitative insights into the Na^+ environments (Figure 1B). The experimental ^{23}Na NMR spectrum of MONT displayed only a fully hydrated Na^+ environment at 93% RH, represented by a sharp peak at approximately −1.3 ppm (Figure 1B). At 75% RH, the ^{23}Na NMR spectrum of MONT revealed two additional Na^+ populations: 11% of Na^+ in an outer-sphere complexation or partially hydrated (at approximately −11 ppm) and 24% as inner-sphere dehydrated Na^+ (at approximately −24 ppm) (Figure 1B). At 55% RH, the spectrum exhibited a large population of outer-sphere/partially hydrated Na^+ (63%) and an increased fraction of dehydrated Na^+ (31%) (Figure 1B). At near 50% RH condition, the ^{23}Na NMR spectrum of Na-hectorite was reported to have bimodal peak shapes, and the peak positions were within a 4 ppm margin of error between studies.[40] At 33% RH, the fraction of dehydrated Na^+ population further increased to 47%, and this fraction only increased to 53% at 11% RH (Figure 1B). Our 11% RH MONT spectrum also concurred with a prior study on dry Na-MONT with near-identical peak position and shape.[47] In sum, our quantitative analysis revealed that only a minimal amount of fully hydrated Na^+ signal (5%) remained by 55% RH, despite the observation that the large-sized nanopore was still 63% of the nanopore size distribution as determined from the XRD data (Figure 1A,B).

To investigate further water behavior during this transition directly, TGA−MS was conducted. Informed by prior TGA and TGA−MS investigation of MONT,[49,51,55,56] the following temperature ranges were designated for monitoring loss of specific water populations along the temperature gradient: loss of freely exchangeable waters including unconfined or excess surface water at T = 25−40 °C, loss of loosely bound waters including mineral-associated waters or cation hydration waters

https://doi.org/10.1021/acs.jpcc.1c05462
J. Phys. Chem. C 2021, 125, 26552−26565

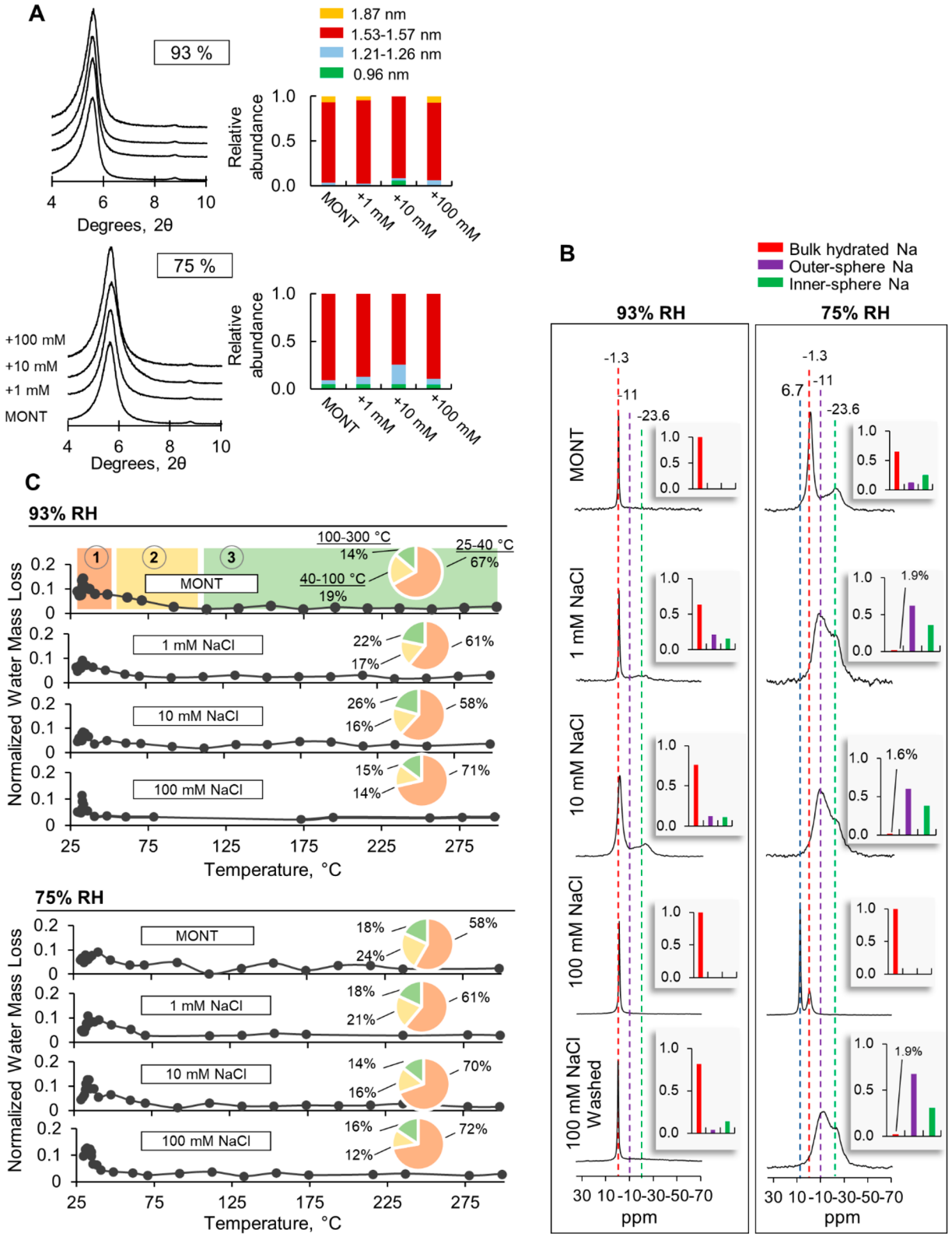

Figure 3. Effects of exogenous NaCl at high-moisture conditions. (A) X-ray diffraction profiles and modeling of nanopore distribution, at 93% RH and 75% RH, for Na-MONT with and without added NaCl (1, 10, or 100 mM NaCl). The different interlayer sizes used in the modeling are represented by green bars (0.96 nm), light blue bars (1.21−1.26 nm), dark red bars (1.53−1.57 nm), and yellow bars (1.87 nm). (B) RH-dependent solid-state ^{23}Na NMR resonances. Washed sample represents MONT loaded with 100 mM NaCl with an additional washing procedure. The bar graph distribution for MONT loaded with 100 mM NaCl is shown fitted without the 6.7 ppm signal of crystalline NaCl. (C) Categorizing water populations through monitoring abundance of water ion at m/z 18. Spectra were sectioned into freely exchangeable waters (water loss at T = 25−40 °C), loosely bound waters (water loss at T = 40−100 °C, and tightly bound waters (water loss at T = 100−300 °C) and normalized for structural OH loss (at T = 300−800 °C). Pie charts show the percent of the total 25−300 °C normalized mass loss within each section. Y-axis reflects normalized mass loss in mg.

https://doi.org/10.1021/acs.jpcc.1c05462
J. Phys. Chem. C 2021, 125, 26552−26565

at T = 40−100 °C, and loss of tightly bound waters on the mineral surface including directly bound cation hydration water at T = 100−300 °C (Figure 1C; SI Figures E−I; SI Table D). Previously,[7] we have reported that the water content during dehydration of the same Na-MONT was from 97% RH to 11% RH. At the specific RH conditions in the present study, the following water content was recorded:[7] ∼900 mg of H_2O per g of clay at 93% RH, ∼342 mg of H_2O per g of clay at 75% RH, ∼117 mg of H_2O per g of clay at 55% RH, and ∼14 mg of H_2O per g of clay at 11% RH. Due to the challenge of determining with high accuracy the mass of the sample in the sample container during the TGA−MS measurements, the mass loss from the different water populations (from 25 to 40 °C) was normalized by the loss of structural OH from the mineral content in the sample. On the basis of the aforementioned 64-fold decrease in the water content from 93% to 11% RH,[7] we expected a significant increase in the relative proportion of tightly bound waters versus freely exchangeable waters in the water populations.

Remarkably, our TGA−MS analysis of MONT alone at all RH conditions revealed that freely exchanged waters (52−67%) accounted for the majority of water loss and the population of loosely bound waters (19−26%) was the second most abundant (Figure 1C). However, the relative proportions of the water populations were dependent on the moisture condition (Figure 1C). At the highest moisture condition (93% RH), 67% of the total water loss was freely exchanged waters, but this fraction dropped to 52% at the lowest RH condition (11%) (Figure 1C). This 22% reduction in freely exchangeable water determined by TGA−MS analysis from 93% RH to 11% RH was 4-fold less than the corresponding 88% decrease in the abundance of large-sized pores (presumed to be populated primarily by freely exchangeable waters) determined by the RH-dependent XRD and was not consistent with the total loss of fully hydrated Na^+ as captured by the ^{23}Na NMR data (Figure 1A−C). The TGA−MS data thus implied overlapping behavior of water populations beyond the demarcated temperature ranges for freely exchangeable, loosely bound, and tightly bound waters. Our results thus concurred with the proposal that external and interlayer trapped moisture may be lost simultaneously during TGA monitoring of water loss from smectite minerals.[55] We note that our dehydrated TGA−MS data exhibited water loss at lower temperatures than a previous study,[56] a discrepancy that we attributed to the extensive heat treatment (20 h at 200 °C), extensive purification procedure, or altered TGA−MS method of the prior study (heating rate of 10 °C/min instead of 20 °C/min as was used here).

To evaluate the effects of Na^+ loading on the application of ^{23}Na NMR as a probe of smectite hydration, experiments were conducted with added exogenous NaCl (1, 10, or 100 mM solution concentration) to slurries of the natural MONT. We also conducted XRD and TGA−MS analyses on these samples to capture subsequent changes in the hydration environment in these NaCl-loaded conditions.

NaCl-Facilitated Dehydration of MONT within Unaltered Nanopore Sizes at High Moisture Conditions. At the high RH conditions (93% and 75% RH), the addition of NaCl (1−100 mM) caused minimal to no changes in the XRD profiles of the MONT samples, as observed by the narrow and symmetrical peaks that implied homogeneous nanopore distributions (Figure 3A; Table 2). In fact, large-sized nanopores (mineral interlayer size of 1.53−1.57 nm) constituted between 75% and 93% of the MONT nanopores in the presence or absence of NaCl (Figure 3A). We subsequently applied ^{23}Na NMR spectroscopy to investigate the potential differences in the MONT hydration conditions induced by NaCl loading that were not revealed by nanopore size dynamics.

Table 2. Results from Experimental X-ray Diffraction Patterns of MONT Loaded with NaCl[a]

	NaCl (mM)	d_{001}	Δd	fwhm
93% RH	0	1.59		0.587
	1	1.59	0.0070	0.519
	10	1.58	0.011	0.537
	100	1.58	0.015	0.562
75% RH	0	1.57		0.590
	1	1.56	0.010	0.592
	10	1.55	0.026	0.727
	100	1.56	0.014	0.615
55% RH	0	1.52		0.860
	1	1.51	0.0070	0.962
	10	1.38	0.14	1.71
	100	1.28	0.24	0.827
11% RH	0	1.16		1.01
	1	1.15	0.012	0.919
	10	1.10	0.065	1.24
	100	1.03	0.13	1.12

[a]RH, relative humidity (RH) for *in situ* moisture-dependent X-ray diffraction measurements; fwhm, full width at half-maximum (2θ°); d_{001}, the basal spacing of the clay layers shown in nm; Δd, difference in interlayer spacing relative to the control MONT (nm).

At 93% RH, the ^{23}Na NMR spectra revealed bulk hydrated Na^+ was dominant (greater than 63% of the total Na) for MONT with or without exogenous NaCl of any concentration (Figure 3B). An increase in exogenous NaCl (1 and 10 mM NaCl) reduced the proportion of the freely hydrated Na^+ resonance in samples equilibrated below 93% RH (Figure 3B). For instance, 65% of the Na^+ was bulk hydrated at 75% RH in the natural Na-MONT, but less than 2% of this population remained when MONT was reacted with 1 mM or 10 mM NaCl (Figure 3B). An increase in both outer-sphere (60−62%) and inner-sphere (36−38%) Na^+ accompanied this decrease in bulk hydrated Na^+ (Figure 3C). Furthermore, at the highest NaCl concentration of 100 mM at 75% RH, there was a new ^{23}Na NMR resonance at 6.7 ppm, which was confirmed to be the crystalline form of NaCl (Figure 3B; SI Figures B and C; SI Tables B, C, and E; SI Figures K−O). Excluding this crystalline NaCl resonance in the quantitative analysis of the hydrated Na^+ populations, we found that MONT loaded with 100 mM NaCl was the only condition apart from MONT alone that displayed the bulk hydrated Na^+ population resonance at 75% RH (Figure 3B). This latter finding implied a partitioning effect whereby only the bulk hydrated Na^+ remained after the dehydrated Na^+ populations (outer-sphere and inner-sphere bound Na) became crystallized on the MONT surface (Figure 3B). Our ^{23}Na NMR spectra at 75% RH showed greater resolution than prior reports on Na-MONT with moisture contents between 26% and 12% water by weight, where only a single, broad resonance was observed.[80]

Following washing of MONT loaded with the highest NaCl concentration (100 mM NaCl), the ^{23}Na NMR spectrum no longer exhibited the crystalline NaCl resonance at 75% RH (Figure 3B). Prior work has shown that washing illite and

https://doi.org/10.1021/acs.jpcc.1c05462
J. Phys. Chem. C 2021, 125, 26552−26565

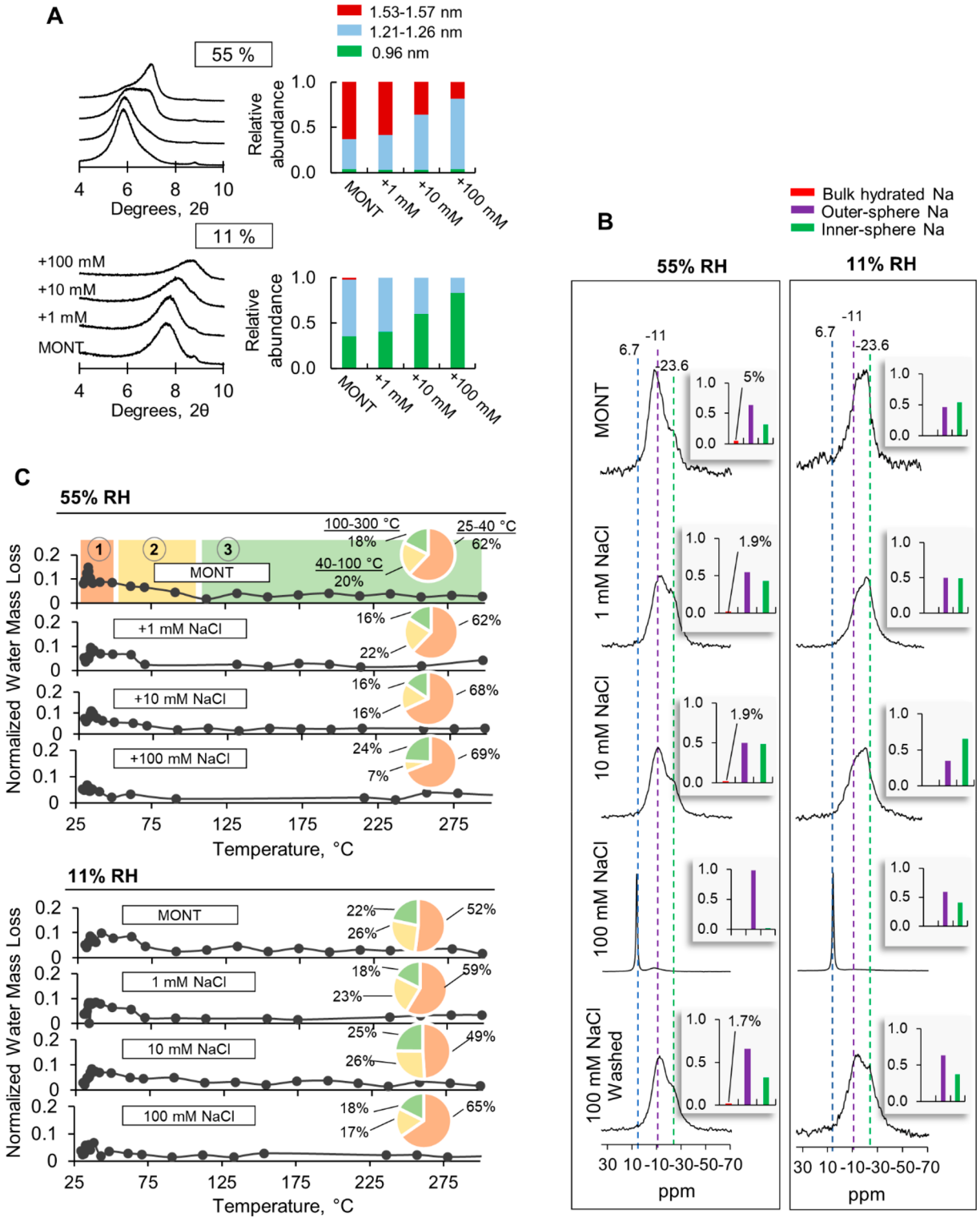

Figure 4. Effects of exogenous NaCl at low-moisture conditions. (A) X-ray diffraction profiles and modeling of nanopore distribution, at 33% RH and 11% RH, for Na-MONT with and without added NaCl (1, 10, or 100 mM NaCl). The different interlayer sizes used in the modeling are represented by green bars (0.96 nm), light blue bars (1.21−1.26 nm), and dark red bars (1.53−1.57 nm). (B) RH-dependent solid-state ^{23}Na NMR resonances. Washed sample represents MONT loaded with 100 mM NaCl with an additional washing procedure. The bar graph distribution for MONT loaded with 100 mM NaCl is shown fitted without the 6.7 ppm signal of crystalline NaCl. (C) Categorizing water populations through monitoring abundance of water ion at m/z 18. Spectra were sectioned into freely exchangeable waters (water loss at T = 25−40 °C), loosely bound waters (water loss at T = 40−100 °C, and tightly bound waters (water loss at T = 100−300 °C) and normalized for structural OH loss (at T = 300−800 °C). Pie charts show the percent of the total 25−300 °C normalized mass loss within each section. Y-axis reflects normalized mass loss in mg.

https://doi.org/10.1021/acs.jpcc.1c05462
J. Phys. Chem. C 2021, 125, 26552−26565

kaolinite with DI water after they were loaded with 100 mM NaCl was sufficient to remove the NaCl peak at 35% RH.[39] Interestingly, at 75% RH, the subsequent ^{23}Na NMR spectrum after the washing procedure closely resembled the NMR spectrum obtained with the MONT samples prepared with relatively lower NaCl concentrations (10 mM) instead of the NMR spectrum of the control MONT, implying that it may be difficult to remove completely tightly bound Na^+ with washing or that the washing process removed some of the indigenous Ca and K cations from the MONT matrix (Figure 3B). Accordingly, our quantitative analysis determined that, at 75% RH, only 1.9% of the ^{23}Na NMR signal in the washed MONT was attributed to the bulk hydrated Na^+ environment whereas the MONT alone spectrum contained 65% (Figure 3B). In agreement with ^{23}Na NMR data, XRD data of the washed sample were in close agreement with the XRD data for MONT samples prepared with 10 mM NaCl (SI Figure A; SI Table A).

We also explored the influence of NaCl concentration on the water populations in MONT as determined by TGA−MS analysis at both 75% and 93% RH (Figure 3). In contrast to the high variability in the abundance of the bulk hydrated Na^+ in the ^{23}Na NMR spectra induced by NaCl loading, the TGA−MS analysis revealed that the proportion of freely exchanged waters only varied by 4−9% across NaCl conditions. The low variability shown by the TGA−MS spectra with different NaCl loading agreed with the relatively unchanged nanopore size distributions seen in the RH-dependent XRD data (Figure 3C). The TGA−MS data revealed moderate effects of exogenous NaCl on the relative abundance of loosely bound water (i.e., water loss between 40 and 100 °C) (Figure 3C). At 93% RH, loosely bound water was decreased from 19% of total in MONT alone to 14% in MONT loaded with 100 mM NaCl (Figure 3C). At 75% RH, the change induced by NaCl was more pronounced, with the proportion of loosely bound water decreasing from 24% in MONT alone to 12% in MONT loaded with 100 mM NaCl (Figure 3C). In sum, ^{23}Na NMR, XRD, and TGA−MS data revealed that the addition of NaCl caused only minor changes in MONT hydration environments at 93% RH (Figure 3). However, at 75% RH, the ^{23}Na NMR data revealed a pronounced decrease in hydrated Na^+ environments within MONT samples with NaCl addition; changes to the XRD nanopore size distributions and TGA−MS water monitoring data were less prominent than those revealed by ^{23}Na NMR (Figure 3).

NaCl-Induced Changes to Nanopore Collapse and Mineral Dehydration at Low Moisture Conditions. Moisture-controlled XRD revealed MONT nanopores underwent major changes when exposed to low moisture conditions (Figure 4A). At 55% RH, 63% of the nanopores in MONT alone were large-sized (∼1.55 nm) nanopores (Figure 4A). With increasing exogenous NaCl, the proportion of the medium-sized (∼1.23 nm) nanopores also increased (Figure 4A). At 55% RH, the abundance of the large-sized nanopore decreased from 63% in MONT alone to only 18% in the sample prepared with the highest Na^+ concentration (100 mM NaCl) (Figure 4A). For the lowest moisture condition (11% RH), MONT loaded with 100 mM NaCl had the greatest abundance of dehydrated, small-sized nanopores (83%), compared to 60% with 10 mM NaCl and 40−42% with 1 mM NaCl or the reference MONT (Figure 4A). The XRD profiles also revealed that NaCl-loaded samples had 001 peaks shifted to higher 2θ values than those of MONT alone and that the shift was proportional to the concentration of NaCl (Figure 4A). Accordingly, MONT loaded with 100 mM NaCl revealed an interlayer spacing 0.24 nm less than that of MONT alone at 55% RH and 0.13 nm less at 11% RH (Table 2). These differences led to, at 55% RH, a shift from primarily large-sized nanopores (∼1.55 nm, 63%) in MONT alone to medium-sized pores (∼1.23 nm, 17%) with 100 mM NaCl and, at 11% RH, a shift from primarily medium-sized nanopores (∼1.23 nm, 63%) in MONT alone to small-sized nanopores (<0.96 nm, 16%) with 100 mM NaCl (Figure 4A).

The hydration environment of Na^+ probed via ^{23}Na NMR primarily comprised outer-sphere and inner-sphere complexed Na^+ at 55% RH for all conditions (Figure 4B; SI Figure A; SI Table A). At 55% RH, MONT loaded with 1 mM exogenous NaCl revealed 43% of Na^+ populations were inner-sphere complexed Na, while 55% were attributed to outer-sphere Na^+ (Figure 4B). Further, the ^{23}Na NMR spectrum of MONT loaded with 10 mM NaCl revealed the greatest fraction of inner-sphere, dehydrated Na^+ at 55% RH (48% of total signal), compared to only 32% in MONT alone (Figure 4B). When the spectrum of MONT prepared with 100 mM NaCl at 55% RH was analyzed without the crystalline NaCl peak, effectively only the outer-sphere complexed Na^+ resonance remained, accounting for 98.4% of total signal (Figure 4B). Thus, again a partitioning effect was exhibited by the 100 mM NaCl sample such that, when analyzed without the crystalline NaCl, the resonance contained less dehydrated (inner-sphere) Na^+ populations (only 1.6%) compared to loadings of 1 or 10 mM NaCl which had 43% and 48% inner-sphere complexed Na, respectively, or even compared to MONT alone with 32% inner-sphere Na^+ (Figure 4B). Following washing of the sample prepared with 100 mM NaCl, the resulting ^{23}Na NMR spectrum at 55% RH exhibited a 2:1 ratio of the fraction of outer-sphere Na^+ to inner-sphere Na, compared to nearly 1:0 in unwashed MONT loaded with 100 mM NaCl, 1:1 in MONT loaded with 10 mM NaCl, about 5:4 in MONT loaded with 1 mM NaCl, and 2:1 in MONT alone (Figure 4B). Therefore, at 55% RH, the environment of Na^+ in MONT loaded with 100 mM NaCl postwashing was found to be most congruent to the environment within the MONT alone sample (without a washing step) (Figure 4B). At 11% RH, all samples unveiled a greater proportion of inner-sphere complexed Na^+ than the corresponding samples at 55% RH, and no bulk hydrated Na^+ was detected for any sample at 11% RH (Figure 4B). In accordance with results from 55% RH, MONT loaded with 10 mM NaCl had the largest fraction of inner-sphere complexed Na^+ at 11% RH (Figure 4B). The amount of inner-sphere Na^+ in the MONT sampled loaded with 10 mM NaCl was 65%, a 17% increase from the amount of inner-sphere Na^+ in MONT alone, 23% larger than in MONT loaded with 1 mM NaCl, and 37% larger than in MONT loaded with 100 mM NaCl (Figure 4B). At 11% RH, the MONT samples loaded with 100 mM NaCl postwashing had 63% of Na^+ in an outer-sphere conformation (Figure 4B). However, the spectrum of MONT alone at 11% RH revealed 46% of the signal to be outer-sphere Na^+ while the fraction of outer-sphere Na^+ was 50% in MONT loaded with 1 mM NaCl, 35% with 10 mM NaCl, and 59% with 100 mM NaCl (Figure 4B).

In sum, ^{23}Na NMR data analysis revealed, at low moisture conditions (11% and 55% RH), the addition of exogenous NaCl (1 and 10 mM) induced an up to 33% greater proportion of inner-sphere complexed Na^+ than exhibited by MONT alone (Figure 4B). However, the spectrum of MONT loaded with 100 mM NaCl exhibited a decrease of up to 97% in the

https://doi.org/10.1021/acs.jpcc.1c05462
J. Phys. Chem. C 2021, 125, 26552−26565

fraction of inner-sphere Na^+ compared to other conditions at 11% and 55% RH (Figure 4B). These results suggest that the loading of exogenous NaCl promotes dehydration until the threshold of crystalline NaCl precipitation, after which a greater fraction of hydrated resonances was revealed.

The TGA−MS data collected at 55% RH revealed that when MONT was loaded with 100 mM exogenous NaCl, a 65% decrease in the amount of loosely bound water was observed (Figure 4C). The amount of loosely bound water in MONT loaded with 100 mM NaCl was also 56% less than in 10 mM NaCl and 68% less than in MONT loaded with 1 mM NaCl (Figure 4C). Interestingly, at 55% RH, the decrease in loosely bound water corresponded to a smaller but appreciable increase in the fraction of freely exchangeable waters for high NaCl conditions; the amount of freely exchangeable water was approximately 9.5% higher in the 10 and 100 mM loaded samples compared to that in MONT alone and MONT loaded with 1 mM NaCl (Figure 4C). The fraction of tightly bound water was found to vary from 16% to 24% for all samples but did not show a NaCl-loading induced trend of either increase or decrease at 55% RH (Figure 4C). The decrease in the proportion of loosely bound waters with increasing exogenous NaCl loading was more dramatic at 55% RH where the addition of 100 mM NaCl on MONT was reflected by a 65% decrease in the amount of loosely bound waters compared to that at 11% RH, where only a 34% decrease was exhibited (Figure 4C). At 11% RH, there was also a less pronounced influence of 1 and 10 mM NaCl loading on the amount of loosely bound water compared with that at 55% such that there was no change in the proportion of loosely bound waters with the addition of 10 mM NaCl and only a 12% difference with the addition of 1 mM NaCl compared to MONT alone (Figure 4C). Neither the freely exchangeable water populations nor the tightly bound water population showed NaCl-loading dependence at 11% RH but comprised between 49% and 65% and 18−25% of total waters, respectively (Figure 4C). Thus, for the TGA analysis, it was concluded that the proclivity of exogenous NaCl to modify the proportions of MONT hydration waters was greater at higher RH conditions. Due to lack of published prior studies on these conditions, it was not possible to perform a comparative analysis with previous data for our samples loaded with exogenous NaCl under different humidity regimes.

CONCLUSION

Here, our objective was to use both ^{23}Na NMR and TGA−MS to obtain quantitative information on the water populations in a hydrated natural Na-MONT and to interpret our data in relation to the interlayer nanopore environments predicted by RH-dependent XRD data. Our first hypothesis was that dehydration of the smectite matrices would lead to a shift in the Na^+ populations in MONT from hydrated Na^+ to inner-sphere Na^+ complexed on the mineral surface. In accordance with this hypothesis, the ^{23}Na NMR data revealed that the fully hydrated Na^+ environment was the primary (over 65%) Na^+ population at 93% RH and 75% RH, whereas at 55% RH, outer-sphere Na^+ was dominant (63%), and a near 1:1 ratio of outer-sphere to inner-sphere (mineral-bound) Na^+ was present at both 33% RH and 11% RH. Our second hypothesis was that the dehydration of the MONT matrix would reduce interlayer spacing (i.e., induce nanopore collapse) and promote trapping of hydration waters within MONT. Along with the dehydration-induced nanopore collapse between 93% RH and 11% RH characterized by a shift from 90% large-sized nanopores at ∼1.55 nm d_{001} to 63% small-sized nanopores at less than 0.96 nm d_{001}, the analysis of MONT water populations through TGA−MS data did uncover a 57% increase in tightly mineral-bound waters but only a 22% of decrease in the amount of freely exchanged waters expected to be maintained primarily in large-sized nanopores. At 11% RH, nearly half of the water populations were found to be freely exchangeable waters. Therefore, collectively, the TGA−MS and ^{23}Na NMR data captured unique behavior of water populations, which were not predictable from the XRD nanopore size dynamics, including revealing the persistence of highly hydrated environments even in the case of significant interlayer nanopore collapse at low RH conditions. Compared to the reference natural MONT, the presence of added exogenous NaCl induced nanopore collapse, accompanied by the transition of partially hydrated Na^+ into crystalline NaCl shown by the ^{23}Na NMR and a reduction in loosely bound water population determined by the TGA-MS data; washed samples were able to recover most of the spectroscopic signatures of the natural MONT. In conclusion, our work offers new insights regarding the hydration environments in smectite nanopores using complementary quantitative spectroscopic approaches, which can be used to probe hydration dynamics in smectite-containing or related mineral matrices with varying chemical composition.

ASSOCIATED CONTENT

Supporting Information

The Supporting Information is available free of charge at https://pubs.acs.org/doi/10.1021/acs.jpcc.1c05462.

Results from XRD, TGA−MS, line fit models, and NMR (PDF)

AUTHOR INFORMATION

Corresponding Author

Ludmilla Aristilde − *Department of Civil and Environmental Engineering, McCormick School of Engineering and Applied Science, Northwestern University, Evanston, Illinois 60208, United States; Department of Biological and Environmental Engineering, Cornell University, Ithaca, New York 14853, United States;* orcid.org/0000-0002-8566-1486; Email: ludmilla.aristilde@northwestern.edu

Authors

Sabrina E. Kelch − *Department of Soil and Crop Sciences, School of Integrative Plant Science, Cornell University, Ithaca, New York 14853, United States; Department of Civil and Environmental Engineering, McCormick School of Engineering and Applied Science, Northwestern University, Evanston, Illinois 60208, United States*

Randall E. Youngman − *Science and Technology Division, Corning Incorporated, Corning, New York 14831, United States;* orcid.org/0000-0002-6647-9865

Eric Ferrage − *Institut de Chimie des Milieux et Matériaux de Poitiers (IC2MP-Hydrasa), UMR 7285 CNRS-Université de Poitiers, 86073 Poitiers, France*

Jade J. Basinski − *Department of Civil and Environmental Engineering, McCormick School of Engineering and Applied Science, Northwestern University, Evanston, Illinois 60208, United States*

Jiaxing Wang − *Department of Civil and Environmental Engineering, McCormick School of Engineering and Applied Science, Northwestern University, Evanston, Illinois 60208, United States*

Complete contact information is available at: https://pubs.acs.org/10.1021/acs.jpcc.1c05462

Notes

The authors declare no competing financial interest.

■ ACKNOWLEDGMENTS

Graduate support for S.E.K. was provided by a National Science Foundation grant awarded to L.A. (Grant NSF CHE 1646815). This work made use of the IMSERC PCM facility at Northwestern University, which has received support from the Soft and Hybrid Nanotechnology Experimental (SHyNE) Resource (Grant NSF ECCS-2025633) and from Northwestern University. We thank both Dr. Christos Malliakas and Dr. Yuyang Wu of the IMSERC facility at Northwestern for their experimental guidance and technical expertise. We also acknowledge Corning Inc. for the use of their facility and their encouragement of academic partnerships.

■ REFERENCES

(1) Schulze, D. G. Clay Minerals. In *Encyclopedia of Soils in the Environment*; Elsevier, 2005; pp 246−254, .

(2) Sposito, G. *The Chemistry of Soils*, 2nd ed.; Oxford University Press, 2008; DOI: 10.1017/CBO9781107415324.004.

(3) Jackson, M. L. Frequency Distribution of Clay Minerals in Major Great Soil Groups as Related to the Factors of Soil Formation. *Clays Clay Miner.* **1957**, *6* (1), 133−143.

(4) Hazen, R. M.; Sverjensky, D. A.; Azzolini, D.; Bish, D. L.; Elmore, S. C.; Hinnov, L.; Milliken, R. E. Clay Mineral Evolution. *Am. Mineral.* **2013**, *98* (11−12), 2007.

(5) Aristilde, L.; Galdi, S. M.; Kelch, S. E.; Aoki, T. G. Sugar-Influenced Water Diffusion, Interaction, and Retention in Clay Interlayer Nanopores Probed by Theoretical Simulations and Experimental Spectroscopies. *Adv. Water Resour.* **2017**, *106*, 24−38.

(6) Okaikue-Woodi, F. E. K.; Kelch, S. E.; Schmidt, M. P.; Enid Martinez, C.; Youngman, R. E.; Aristilde, L. Structures and Mechanisms in Clay Nanopore Trapping of Structurally-Different Fluoroquinolone Antimicrobials. *J. Colloid Interface Sci.* **2018**, *513*, 367−378.

(7) Kelch, S. E.; Ferrage, E.; Lanson, B.; Charlet, L.; Aristilde, L. Water Trapping Dynamics in Carbohydrate-Populated Smectite Interlayer Nanopores. *J. Phys. Chem. C* **2019**, *123* (47), 28816−28827.

(8) Zhu, R.; Chen, Q.; Zhou, Q.; Xi, Y.; Zhu, J.; He, H. Adsorbents Based on Montmorillonite for Contaminant Removal from Water: A Review. *Appl. Clay Sci.* **2016**, *123*, 239.

(9) Kausar, A.; Iqbal, M.; Javed, A.; Aftab, K.; Nazli, Z. i. H.; Bhatti, H. N.; Nouren, S. Dyes Adsorption Using Clay and Modified Clay: A Review. *J. Mol. Liq.* **2018**, *256* (March), 395−407.

(10) Schoonheydt, R. A. Smectite-Type Clay Minerals as Nanomaterials. *Clays Clay Miner.* **2002**, *50* (4), 411−420.

(11) Awad, A. M.; Shaikh, S. M. R.; Jalab, R.; Gulied, M. H.; Nasser, M. S.; Benamor, A.; Adham, S. Adsorption of Organic Pollutants by Natural and Modified Clays: A Comprehensive Review. *Sep. Purif. Technol.* **2019**, *228* (June), 115719.

(12) Siantar, D. P.; Feinberg, B. A.; Fripiat, J. J. Interaction between Organic and Inorganic Pollutants in the Clay Interlayer. *Clays Clay Miner.* **1994**, *42* (2), 187−196.

(13) Ferrage, E.; Lanson, B.; Sakharov, B. A.; Geoffroy, N.; Jacquot, E.; Drits, V. A. Investigation of Dioctahedral Smectite Hydration Properties by Modeling of X-Ray Diffraction Profiles: Influence of Layer Charge and Charge Location. *Am. Mineral.* **2007**, *92* (10), 1731−1743.

(14) Ferrage, E. Investigation of the Interlayer Organization of Water and Ions in Smectite from the Combined Use of Diffraction Experiments and Molecular Simulations. A Review of Methodology, Applications, and Perspectives. *Clays Clay Miner.* **2016**, *64* (4), 348−373.

(15) Ferrage, E.; Sakharov, B. A.; Michot, L. J.; Delville, A.; Bauer, A.; Lanson, B.; Grangeon, S.; Frapper, G.; Jiménez-Ruiz, M.; Cuello, G. J. Hydration Properties and Interlayer Organization of Water and Ions in Synthetic Na-Smectite with Tetrahedral Layer Charge. Part 2. Toward a Precise Coupling between Molecular Simulations and Diffraction Data. *J. Phys. Chem. C* **2011**, *115* (5), 1867−1881.

(16) Holmboe, M.; Bourg, I. C. Molecular Dynamics Simulations of Water and Sodium Diffusion in Smectite Interlayer Nanopores as a Function of Pore Size and Temperature. *J. Phys. Chem. C* **2014**, *118* (2), 1001−1013.

(17) Bourg, I. C.; Ajo-Franklin, J. B. Clay, Water, and Salt: Controls on the Permeability of Fine-Grained Sedimentary Rocks. *Acc. Chem. Res.* **2017**, *50* (9), 2067−2074.

(18) Tertre, E.; Delville, A.; Prêt, D.; Hubert, F.; Ferrage, E. Cation Diffusion in the Interlayer Space of Swelling Clay Minerals - A Combined Macroscopic and Microscopic Study. *Geochim. Cosmochim. Acta* **2015**, *149*, 251.

(19) Churakov, S. V. Mobility of Na and Cs on Montmorillonite Surface under Partially Saturated Conditions. *Environ. Sci. Technol.* **2013**, *47* (17), 9816.

(20) Boţan, A.; Rotenberg, B.; Marry, V.; Turq, P.; Noetinger, B. Hydrodynamics in Clay Nanopores. *J. Phys. Chem. C* **2011**, *115* (32), 16109−16115.

(21) Brigatti, M. F.; Galán, E.; Theng, B. K. G. Structure and Mineralogy of Clay Minerals. In *Developments in Clay Science*; Bergaya, F., Gerhard, L., Eds.; Newnes, 2013; Vol. *5*, Chapter 2, pp 21−81.

(22) Dazas, B.; Lanson, B.; Breu, J.; Robert, J. L.; Pelletier, M.; Ferrage, E. Smectite Fluorination and Its Impact on Interlayer Water Content and Structure: A Way to Fine Tune the Hydrophilicity of Clay Surfaces? *Microporous Mesoporous Mater.* **2013**, *181*, 233.

(23) Holmboe, M.; Bourg, I. C. Molecular Dynamics Simulations of Water and Sodium Diffusion in Smectite Interlayer Nanopores as a Function of Pore Size and Temperature. *J. Phys. Chem. C* **2014**, *118* (2), 1001−1013.

(24) Yeşilbaş, M.; Holmboe, M.; Boily, J. F. Cohesive Vibrational and Structural Depiction of Intercalated Water in Montmorillonite. *ACS Earth and Space Chemistry* **2018**, *2* (1), 38−47.

(25) Ferrage, E.; Lanson, B.; Sakharov, B. A.; Geoffroy, N.; Jacquot, E.; Drits, V. A. Investigation of Dioctahedral Smectite Hydration Properties by Modeling of X-Ray Diffraction Profiles: Influence of Layer Charge and Charge Location. *Am. Mineral.* **2007**, *92* (10), 1731−1743.

(26) Ferrage, E.; Tournassat, C.; Rinnert, E.; Lanson, B. Influence of PH on the Interlayer Cationic Composition and Hydration State of Ca-Montmorillonite: Analytical Chemistry, Chemical Modelling and XRD Profile Modelling Study. *Geochim. Cosmochim. Acta* **2005**, *69* (11), 2797−2812.

(27) Hatch, C. D.; Wiese, J. S.; Crane, C. C.; Harris, K. J.; Kloss, H. G.; Baltrusaitis, J. Water Adsorption on Clay Minerals as a Function of Relative Humidity: Application of BET and Freundlich Adsorption Models. *Langmuir* **2012**, *28* (3), 1790−1803.

(28) Berend, I.; Cases, J. M.; Francois, M.; Uriot, J. P.; Michot, L. J.; Masion, A.; Thomas, F. Mechanism of Adsorption and Desorption of Water Vapor by Homoionic Montmorillonites: 2. The Li^+ Na^+, K^+, Rb^+ and Cs^+-Exchanged Forms. *Clays Clay Miner.* **1997**, *45* (3), 324−336.

(29) Lindholm, J.; Boily, J.-F.; Holmboe, M. Deconvolution of Smectite Hydration Isotherms. *ACS Earth Space Chem.* **2019**, *3*, 2490.

(30) Ferrage, E.; Lanson, B.; Michot, L. J.; Robert, J. L. Hydration Properties and Interlayer Organization of Water and Ions in Synthetic Na-Smectite with Tetrahedral Layer Charge. Part 1. Results from X-

Ray Diffraction Profile Modeling. *J. Phys. Chem. C* **2010**, *114* (10), 4515−4526.
(31) Tertre, E.; Ferrage, E.; Bihannic, I.; Michot, L. J.; Prêt, D. Influence of the Ionic Strength and Solid/Solution Ratio on Ca(II)-for-Na+ Exchange on Montmorillonite. Part 2: Understanding the Effect of the m/V Ratio. Implications for Pore Water Composition and Element Transport in Natural Media. *J. Colloid Interface Sci.* **2011**, *363* (1), 334−347.
(32) Svensson, P. D.; Hansen, S. Combined Salt and Temperature Impact on Montmorillonite Hydration. *Clays Clay Miner.* **2013**, *61* (4), 328−341.
(33) Sakharov, B. A.; Naumov, A. S.; Drits, V. A. X-Ray Diffraction by Mixed-Layer Structures with Random Distribution of Stacking Faults. *Dokl. Akad. Nauk SSSR* **1982**, *265*, 339−343.
(34) Ferrage, E.; Lanson, B.; Sakharov, B. A.; Drits, V. A. Investigation of Smectite Hydration Properties by Modeling Experimental X-Ray Diffraction Patterns: Part I: Montmorillonite Hydration Properties. *Am. Mineral.* **2005**, *90* (8−9), 1358−1374.
(35) Yeşilbaş, M.; Holmboe, M.; Boily, J. F. Cohesive Vibrational and Structural Depiction of Intercalated Water in Montmorillonite. *ACS Earth and Space Chemistry* **2018**, *2* (1), 38−47.
(36) Caccamo, M. T.; Mavilia, G.; Mavilia, L.; Lombardo, D.; Magazù, S. Self-Assembly Processes in Hydrated Montmorillonite by FTIR Investigations. *Materials* **2020**, *13* (5), 1100.
(37) Ohkubo, T.; Saito, K.; Kanehashi, K.; Ikeda, Y. A Study on Hydration Behaviors of Interlayer Cations in Montmorillonite by Solid State NMR. *Sci. Technol. Adv. Mater.* **2004**, *5* (5−6), 693−696.
(38) Fonseca, C. G.; Vaiss, V. S.; Wypych, F.; Diniz, R.; Leitão, A. A. Structural and Thermodynamic Investigation of the Hydration-Dehydration Process of Na+-Montmorillonite Using DFT Calculations. *Appl. Clay Sci.* **2017**, *143*, 212.
(39) Kim, Y.; Kirkpatrick, R. J. 23Na And 133Cs NMR Study of Cation Adsorption on Mineral Surfaces: Local Environments, Dynamics, and Effects of Mixed Cations. *Geochim. Cosmochim. Acta* **1997**, *61* (24), 5199−5208.
(40) Aranda, P.; Ruiz-hitzky, E. Poly (Ethylene Oxide) -Silicate Intercalation Materials. *Chem. Mater.* **1992**, *4*, 1395−1403.
(41) Laperche, V.; Lambert, J. F.; Prost, R.; Fripiat, J. J. High-Resolution Solid-State NMR of Exchangeable Cations in the Interlayer Surface of a Swelling Mica: 23Na, 111Cd, and 133Cs Vermiculites. *J. Phys. Chem.* **1990**, *94* (25), 8821−8831.
(42) Nanda, R.; Bowers, G. M.; Loganathan, N.; Burton, S. D.; Kirkpatrick, R. J. Temperature Dependent Structure and Dynamics in Smectite Interlayers: 23Na MAS NMR Spectroscopy of Na-Hectorite. *RSC Adv.* **2019**, *9* (22), 12755−12765.
(43) Bowers, G. M.; Singer, J. W.; Bish, D. L.; Kirkpatrick, R. J. Alkali Metal and H2O Dynamics at the Smectite/Water Interface. *J. Phys. Chem. C* **2011**, *115* (47), 23395−23407.
(44) Casal, B.; Aranda, P.; Sanz, J.; Ruiz-Hitzky, E. Interlayer Adsorption of Macrocyclic Compounds (Crown-Ethers and Cryptands) in 2:1 Phyllosilicates: II. Structural Features. *Clay Miner.* **1994**, *29* (2), 191−203.
(45) Kloprogge, J. T.; Jansen, J. B. H.; Schuiling, R. D.; Geus, J. W. The Interlayer Collapse during Dehydration of Synthetic Na0.7-Beidellite: A 23Na Solid-State Magic-Angle Spinning NMR Study. *Clays Clay Miner.* **1992**, *40* (5), 561−566.
(46) Sanz, J.; Sobrados, I.; Robert, J. Influence of Hydration on 23Na, 27Al, and 29Si MAS-NMR Spectra of Sodium Saponites and Sodium Micas. *Am. Mineral.* **2015**, *100* (5), 1076−1083.
(47) Reinholdt, M. X.; Kirkpatrick, R. J.; Pinnavaia, T. J. Montmorillonite-Poly(Ethylene Oxide) Nanocomposites: Interlayer Alkali Metal Behavior. *J. Phys. Chem. B* **2005**, *109* (34), 16296−16303.
(48) Che, C.; Glotch, T. D.; Bish, D. L.; Michalski, J. R.; Xu, W. Spectroscopic Study of the Dehydration and/or Dehydroxylation of Phyllosilicate and Zeolite Minerals. *J. Geophys. Res.* **2011**, *116* (5), 1−23.
(49) Xie, G.; Xiao, Y.; Deng, M.; Zhang, Q.; Huang, D.; Jiang, L.; Yang, Y.; Luo, P. Quantitative Investigation of the Hydration Behavior of Sodium Montmorillonite by Thermogravimetric Analysis and Low-Field Nuclear Magnetic Resonance. *Energy Fuels* **2019**, *33* (9), 9067−9073.
(50) Teixeira-Neto, Â. A.; Izumi, C. M. S.; Temperini, M. L. A.; Ferreira, A. M. D. C.; Constantino, V. R. L. Hybrid Materials Based on Smectite Clays and Nutraceutical Anthocyanins from the Açaí Fruit. *Eur. J. Inorg. Chem.* **2012**, *2012* (32), 5411−5420.
(51) Xie, W.; Gao, Z.; Liu, K.; Pan, W. P.; Vaia, R.; Hunter, D.; Singh, A. Thermal Characterization of Organically Modified Montmorillonite. *Thermochim. Acta* **2001**, *367* (368), 339−350.
(52) Martins, M. G.; Martins, D. O. T. A.; De Carvalho, B. L. C.; Mercante, L. A.; Soriano, S.; Andruh, M.; Vieira, M. D.; Vaz, M. G. F. Synthesis and Characterization of Montmorillonite Clay Intercalated with Molecular Magnetic Compounds. *J. Solid State Chem.* **2015**, *228*, 99−104.
(53) Sun, B.; Zhang, M.; Zhou, N.; Chu, X.; Yuan, P.; Chi, C.; Wu, F.; Shen, J. Study on Montmorillonite-Chlorhexidine Acetate-Terbinafine Hydrochloride Intercalation Composites as Drug Release Systems. *RSC Adv.* **2018**, *8* (38), 21369−21377.
(54) Tajeddine, L.; Gailhanou, H.; Blanc, P.; Lassin, A.; Gaboreau, S.; Vieillard, P. Hydration-Dehydration Behavior and Thermodynamics of MX-80 Montmorillonite Studied Using Thermal Analysis. *Thermochim. Acta* **2015**, *604*, 83−93.
(55) Foldvari, M. *Handbook of Thermo-Gravimetric System of Minerals and Its Use in Geological Practice*; Occasional Papers of the Geological Institute of Hungary, Vol. 213; Geological Institute of Hungary, 2011.
(56) Środoń, J.; McCarty, D. K. Surface Area and Layer Charge of Smectite from CEC and EGME/H2O-Retention Measurements. *Clays Clay Miner.* **2008**, *56* (2), 155−174.
(57) Clay Mineral Society. Source Clays https://www.clays.org/sourceclays_data/ (accessed Nov 24, 2021).
(58) Jänchen, J.; Bauermeister, A.; Feyh, N.; De Vera, J. P.; Rettberg, P.; Flemming, H. C.; Szewzyk, U. Water Retention of Selected Microorganisms and Martian Soil Simulants under Close to Martian Environmental Conditions. *Planet. Space Sci.* **2014**, *98*, 163−168.
(59) Williams, P. T.; Besler, S. Thermogravimetric Analysis of the Components of Biomass. In *Advances in Thermochemical Biomass Conversion*; Springer: Dordrecht, The Netherlands, 1993; pp 771−783.
(60) Park, Y.; Sun, Z.; Ayoko, G. A.; Frost, R. L. Removal of Herbicides from Aqueous Solutions by Modified Forms of Montmorillonite. *J. Colloid Interface Sci.* **2014**, *415*, 127.
(61) de Paiva, L. B.; Morales, A. R.; Valenzuela Díaz, F. R. Organoclays: Properties, Preparation and Applications. *Appl. Clay Sci.* **2008**, *42* (1−2), 8−24.
(62) Balesdent, J. The Significance of Organic Separates to Carbon Dynamics and Its Modelling in Some Cultivated Soils. *European Journal of Soil Science* **1996**, *47* (4), 485−493.
(63) Greenspan, L. Humidity Fixed Points of Binary Saturated Aqueous Solutions. *J. Res. Natl. Bur. Stand., Sect. A* **1977**, *81A* (1), 89.
(64) *Materials Studio*; BIOVIA, Dassault Systemes: San Diego, CA, 2020.
(65) *Discovery Studio*; BIOVIA, Dassault Systemes: San Diego, CA, 2020.
(66) Cygan, R. T.; Liang, J.-J.; Kalinichev, A. G. Molecular Models of Hydroxide, Oxyhydroxide, and Clay Phases and the Development of a General Force Field. *J. Phys. Chem. B* **2004**, *108* (4), 1255−1266.
(67) Mark, P.; Nilsson, L. Structure and Dynamics of the TIP3P, SPC, and SPC/E Water Models at 298 K. *J. Phys. Chem. A* **2001**, *105* (43), 9954−9960.
(68) Sun, H. COMPASS: An Ab Initio Force-Field Optimized for Condensed-Phase ApplicationsOverview with Details on Alkane and Benzene Compounds. *J. Phys. Chem. B* **1998**, *102* (38), 7338−7364.
(69) Aristilde, L.; Marichal, C.; Miéhé-Brendlé, J.; Lanson, B.; Charlet, L. Interactions of Oxytetracycline with a Smectite Clay: A Spectroscopic Study with Molecular Simulations. *Environ. Sci. Technol.* **2010**, *44* (20), 7839−7845.

(70) Pochodylo, A. L.; Aoki, T. G.; Aristilde, L. Adsorption Mechanisms of Microcystin Variant Conformations at Water-Mineral Interfaces: A Molecular Modeling Investigation. *J. Colloid Interface Sci.* **2016**, *480*, 166−174.
(71) Aristilde, L.; Sposito, G. Molecular modeling of metal complexation by a fluoroquinolone antibiotic. *Environ. Toxicol. Chem.* **2008**, *27* (11), 2304−2310.
(72) Klein, A. R.; Sarri, E.; Kelch, S. E.; Basinski, J. J.; Vaidya, S.; Aristilde, L. Probing the Fate of Different Structures of Beta-Lactam Antibiotics: Hydrolysis, Mineral Capture, and Influence of Organic Matter. *ACS Earth Space Chem.* **2021**, *5* (6), 1511−1524.
(73) Clark, S. J.; Segall, M. D.; Pickard, C. J.; Hasnip, P. J.; Probert, M. I. J.; Refson, K.; Payne, M. C. First Principles Methods Using CASTEP. *Z. Kristallogr. - Cryst. Mater.* **2005**, *220* (5−6), 567−570.
(74) Profeta, M.; Mauri, F.; Pickard, C. J. Accurate First Principles Prediction of 17O NMR Parameters in SiO2: Assignment of the Zeolite Ferrierite Spectrum. *J. Am. Chem. Soc.* **2003**, *125* (2), 541−548.
(75) Sun, H.; Dwaraknath, S.; Ling, H.; Qu, X.; Huck, P.; Persson, K. A.; Hayes, S. E. Enabling Materials Informatics for 29Si Solid-State NMR of Crystalline Materials. *npj Comput. Mater.* **2020**, *6* (1), 1−7.
(76) Perdew, J. P.; Burke, K.; Ernzerhof, M. Generalized Gradient Approximation Made Simple. *Phys. Rev. Lett.* **1996**, *77* (18), 3865−3868.
(77) Pickard, C. J.; Mauri, F. All-Electron Magnetic Response with Pseudopotentials: NMR Chemical Shifts. *Phys. Rev. B: Condens. Matter Mater. Phys.* **2001**, *63* (24), 245101.
(78) Yates, J. R.; Pickard, C. J.; Mauri, F. Calculation of NMR Chemical Shifts for Extended Systems Using Ultrasoft Pseudopotentials. *Phys. Rev. B: Condens. Matter Mater. Phys.* **2007**, *76* (2), 024401.
(79) Sturniolo, S.; Green, T. F. G.; Hanson, R. M.; Zilka, M.; Refson, K.; Hodgkinson, P.; Brown, S. P.; Yates, J. R. Visualization and Processing of Computed Solid-State NMR Parameters: MagresView and MagresPython. *Solid State Nucl. Magn. Reson.* **2016**, *78*, 64.
(80) Ohkubo, T.; Saito, K.; Kanehashi, K.; Ikeda, Y. A Study on Hydration Behaviors of Interlayer Cations in Montmorillonite by Solid State NMR. *Sci. Technol. Adv. Mater.* **2004**, *5* (5−6), 693−696.

NOTE ADDED AFTER ASAP PUBLICATION

This paper was published ASAP on November 26, 2021, with an error in the formula in the Simulated ^{23}Na NMR paragraph, and content missing from Figure 2 caption. The corrected version was reposted on November 29, 2021.

https://doi.org/10.1021/acs.jpcc.1c05462
J. Phys. Chem. C 2021, 125, 26552−26565